Theoretical analysis of spectrally encoded endoscopy

Michal Merman, Avraham Abramov, and Dvir Yelin*

Department of Biomedical Engineering, Technion – Israel Institute of Technology, 32000 Haifa, Israel
*yelin@bm.technion.ac.il

Abstract: Using a single optical fiber and miniature distal optics, spectrally-encoded endoscopy (SEE) has been demonstrated as a promising, three-dimensional endoscopic imaging method with a large number of resolvable points and high frame rates. We present a detailed theoretical study of the SEE prototype system and probe. Several key imaging parameters of SEE are thoroughly derived and formulated, including the three-dimensional point-spread function and field of view, as well as the system's optical aberrations and fundamental limits. We find that the point-spread function of the SEE system maintains a unique relation between its transverse and axial shapes, discuss the asymmetry of the volumetric field of view, determine that the number of lateral resolvable points is nearly twice than what was previously accepted, and derive an expression for the upper limit for the total number of resolvable points in the cross-sectional image plane.

OCIS Codes: (110.2350) Fiber optics imaging; (170.2150) Endoscopic imaging; (110.4850) Optical transfer functions; (110.2990) Image formation theory.

References and Links

1. C. M. Brown, P. G. Reinhall, S. Karasawa, and E. J. Seibel, "Optomechanical design and fabrication of resonant microscanners for a scanning fiber endoscope," Opt. Eng. **45**, 043001-043010 (2006).
2. D. L. Dickensheets, and G. S. Kino, "Silicon-micromachined scanning confocal optical microscope," J. Microelectromech. Syst. **7**, 38–47 (1998).
3. A. L. Polglase, W. J. McLaren, S. A. Skinner, R. Kiesslich, M. F. Neurath, and P. M. Delaney, "A fluorescence confocal endomicroscope for in vivo microscopy of the upper- and the lower-GI tract," in *Digestive Disease Week/105th Annual Meeting of the American-Gastroenterological-Association* (New Orleans, LA, 2004), pp. 686–695.
4. Y. C. Wu, Y. X. Leng, J. F. Xi, and X. D. Li, "Scanning all-fiber-optic endomicroscopy system for 3D nonlinear optical imaging of biological tissues," Opt. Express **17**(10), 7907–7915 (2009).
5. G. J. Tearney, M. Shishkov, and B. E. Bouma, "Spectrally encoded miniature endoscopy," Opt. Lett. **27**(6), 412–414 (2002).
6. D. Yelin, I. Rizvi, W. M. White, J. T. Motz, T. Hasan, B. E. Bouma, and G. J. Tearney, "Three-dimensional miniature endoscopy," Nature **443**(7113), 765 (2006).
7. D. Yelin, S. H. Yun, B. E. Bouma, and G. J. Tearney, "Three-dimensional imaging using spectral encoding heterodyne interferometry," Opt. Lett. **30**(14), 1794–1796 (2005).
8. L. Froehly, S. N. Martin, T. Lasser, C. Depeursinge, and F. Lang, "Multiplexed 3D imaging using wavelength encoded spectral interferometry: a proof of principle," Opt. Commun. **222**, 127–136 (2003).
9. D. Yelin, W. M. White, J. T. Motz, S. H. Yun, B. E. Bouma, and G. J. Tearney, "Spectral-domain spectrally-encoded endoscopy," Opt. Express **15**(5), 2432–2444 (2007).
10. M. A. Choma, M. V. Sarunic, C. H. Yang, and J. A. Izatt, "Sensitivity advantage of swept source and Fourier domain optical coherence tomography," Opt. Express **11**(18), 2183–2189 (2003).
11. J. F. de Boer, B. Cense, B. H. Park, M. C. Pierce, G. J. Tearney, and B. E. Bouma, "Improved signal-to-noise ratio in spectral-domain compared with time-domain optical coherence tomography," Opt. Lett. **28**(21), 2067–2069 (2003).
12. R. Leitgeb, C. Hitzenberger, and A. Fercher, "Performance of fourier domain vs. time domain optical coherence tomography," Opt. Express **11**(8), 889–894 (2003).
13. D. Yelin, B. E. Bouma, N. Iftimia, and G. J. Tearney, "Three-dimensional spectrally encoded imaging," Opt. Lett. **28**(23), 2321–2323 (2003).
14. D. Yelin, B. E. Bouma, and G. J. Tearney, "Volumetric sub-surface imaging using spectrally encoded endoscopy," Opt. Express **16**(3), 1748–1757 (2008).

15. D. Yelin, B. E. Bouma, J. J. Rosowsky, and G. J. Tearney, "Doppler imaging using spectrally-encoded endoscopy," Opt. Express **16**(19), 14836–14844 (2008).
16. B. E. Bouma, and G. J. Tearney, eds., *Handbook of Optical Coherence Tomography* (Marcel Dekker, New York, 2002).
17. M. Wojtkowski, A. Kowalczyk, R. Leitgeb, and A. F. Fercher, "Full range complex spectral optical coherence tomography technique in eye imaging," Opt. Lett. **27**(16), 1415–1417 (2002).
18. K. B. Sung, C. N. Liang, M. Descour, T. Collier, M. Follen, and R. Richards-Kortum, "Fiber-optic confocal reflectance microscope with miniature objective for in vivo imaging of human tissues," IEEE Trans. Biomed. Eng. **49**(10), 1168–1172 (2002).
19. C. Boudoux, S. Yun, W. Oh, W. White, N. Iftimia, M. Shishkov, B. Bouma, and G. Tearney, "Rapid wavelength-swept spectrally encoded confocal microscopy," Opt. Express **13**(20), 8214–8221 (2005).
20. D. Yelin, C. Boudoux, B. E. Bouma, and G. J. Tearney, "Large area confocal microscopy," Opt. Lett. **32**(9), 1102–1104 (2007).
21. D. Yelin, B. E. Bouma, S. H. Yun, and G. J. Tearney, "Double-clad fiber for endoscopy," Opt. Lett. **29**(20), 2408–2410 (2004).

1. Introduction

Endoscopes are widely used in modern medical practice, making clinical procedures less invasive and saving time and cost, while providing physicians with valuable information from within the body. While current state-of-the-art clinical video endoscopes transmit excellent image quality, their overall size is capped by the dimensions of their sensors and electronics. Smaller and more flexible endoscopes have recently become available for clinical practice using optical fiber bundles, where each individual fiber is used to transmit one pixel in an image. Maintaining acceptable image quality with small diameter fiber bundles is challenging, however; each optical fiber has a finite size, and therefore only a limited number of fibers can be packed into an endoscope with a given diameter. Several research groups have attempted to rapidly scan light from an optical fiber to obtain an image [1–4]. While high quality images have been obtained using this technique, the size of the scanning mechanisms make rapid distal scanning difficult to implement in the smallest endoscopic probes.

Recently, a single-fiber imaging technique termed spectrally encoded endoscopy (SEE) was introduced [5], which replaced rapid scanning by spatial spectral encoding. SEE uses a diffraction grating and a miniature lens to generate a spectrally resolved line on the sample, which can be slowly scanned in one dimension to obtain a two-dimensional image with a large number of resolvable points. Reducing the need for rapid scanning within the endoscopic probe allows significant reduction in probe size, essentially trading the bulk and complexity of a rapid scanning mechanism with a more sophisticated optical design, leaving the total probe diameter limited only by the diameter of its optics [6].

Several methods for obtaining three-dimensional imaging in SEE have been proposed, using time [7] and spectral [8,9] domain interferometric techniques. Compared to time-domain interferometry, spectral domain interferometry offers orders-of-magnitude improvement in signal-to-noise ratio (SNR) in optical coherence tomography (OCT), allowing improved imaging quality and speed [10–12]. Spectral-domain SEE has been shown promising for three-dimensional imaging [8,9,13], sub-surface volumetric imaging [14], and Doppler imaging [15].

A fundamental optical analysis of multiplexed three-dimensional imaging using wavelength encoded spectral interferometry was first presented by Froehly *et al.* [8], and various approximated expressions are often being used to estimate the imaging parameters of spectrally encoded endoscopy [5,9]. In this paper, a detailed theoretical analysis of the SEE system [6] is presented in which we account for the effects of the probe's limited circular aperture, its optical aberrations, and the finite resolution of the spectrometer. We first outline and formulate the interferometric SEE working principles, derive the system's point-spread function (PSF) and its three-dimensional field of view using diffraction theory, and study the effect of the various optical aberrations that are present in the system.

2. The SEE system

We consider an interferometric SEE system [6,9,13–15] (Fig. 1), comprised of a broadband light source, a Michelson interferometer, a fast spectrometer, and an optical delay control module at the reference arm. The SEE probe optics [6,14] consist of a gradient-index (GRIN) lens (L1) and a transmission diffraction grating (G), which together generate a spectrally-encoded transverse line illumination on the sample. Each wavelength from the broadband source is diffracted to a distinct angle toward the sample according to:

$$n_p \sin \theta_0 + n_m \sin \theta = m\lambda G, \tag{1}$$

where n_p and n_m denote the refractive indices of the grating substrate and the medium surrounding the probe, respectively, θ_0 and θ are the incidence and the diffraction angles, respectively, m denotes the diffraction order, λ denotes the wavelength and G denotes the grating groove density. Note that Eq. (1) slightly differs from commonly used grating equations to account for the light transition between two different media having different refractive indices. To achieve high angular dispersion, SEE often uses high groove density gratings designed to have high diffraction efficiency only in the first ($m = 1$) diffraction order, which, for simplicity, will be considered throughout this work.
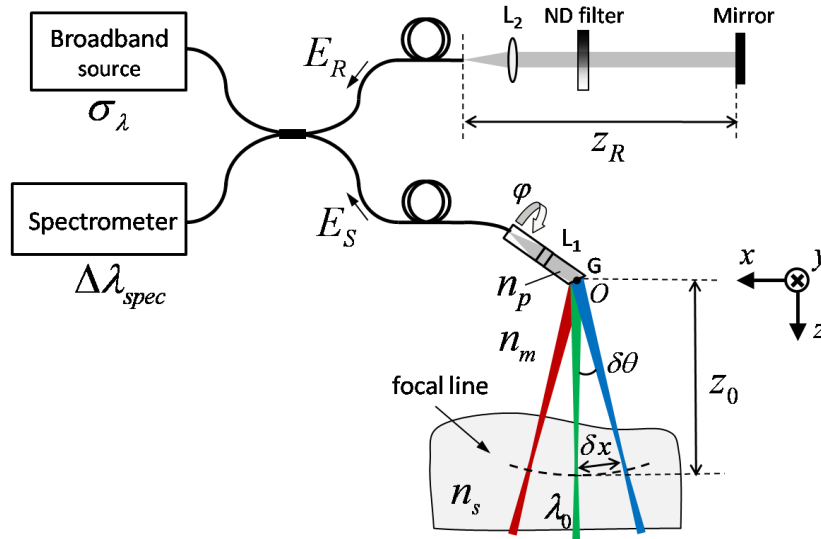

Fig. 1. Schematic of an interferometric spectral domain SEE system (ND – neutral density filter).

We set the origin of the system's coordinates (O) at the center of the diffraction grating, where the positive z axis is pointed at the direction of the diffracted center wavelength λ_0. For small angle difference $\delta\theta$ there is a linear relation between the transverse distance δx at the focal plane and the corresponding wavelength interval $\delta\lambda$, obtained by differentiating Eq. (1) for imaging in air ($n_m = 1$) and substituting $\delta x = z_0 \cdot \delta\theta$:

$$\delta x = \frac{Gz_0}{\cos\theta} \delta\lambda \approx 2\pi \frac{Gz_0}{\cos\theta} \frac{\delta k}{k^2}. \tag{2}$$

where $k = 2\pi/\lambda$ denotes the angular wavenumber and z_0 is the distance from the grating to the focal plane (marked by the curved dashed line in Fig. 1). Each point on the sample along

the spectral line is illuminated by light with spectral bandwidth Δk. In a high quality imaging system with more than hundred resolvable elements per line, we can assume that the spectral bandwidth illuminating each transverse sample location Δk is significantly smaller than the total source bandwidth σ_k, i.e. $\Delta k << \sigma_k$.

Scanning the spectrally encoded line in the perpendicular transverse coordinate (y axis) is accomplished by scanning the angle φ (see Fig. 1), rotating the SEE probe around its optical axis. In recent works a galvanometric scanner (Cambridge Technology, Inc., not shown in Fig. 1) was used for probe rotation, which was limited to a maximum mechanical scanning angle of 20° [6,9]. The third axial dimension is obtained by allowing the light reflected from the sample back into the probe to interfere with light from the reference mirror on a fast linear CCD camera within a high resolution spectrometer.

While several different configurations of SEE could be considered for different applications, we choose to base our analysis on the probe design that was first published in Ref [6]. and was later used in Refs [9,14,15]. While other probe designs may have somewhat different optical parameters and feature sets, they would share many of the imaging principles and limitations of the SEE technique which are derived below.

3. SEE prototype analysis

3.1 Probe structure and components

The SEE probe [6,14,15] [Fig. 2(a)] is comprised of a single-mode optical fiber (125 μm clad diameter), a 1.5 mm long silica cylindrical spacer, a polished 350 μm diameter GRIN lens (ILW-0.35, NSG America, Inc.) and a second 1.5 mm long silica spacer on which a 1000 lines/mm transmission diffraction grating was fabricated (Holographix LLC, Hudson, MA). The angle between the grating's normal and the optical axis is $\theta_0 = 19°$, chosen as the Littrow's angle for the central wavelength $\lambda_0 = 800$ nm for imaging in air [Eq. (1), $n_m = 1$]. The different components are held together using optical grade glue. A photograph of the probe is shown in Fig. 2(b) for reference.
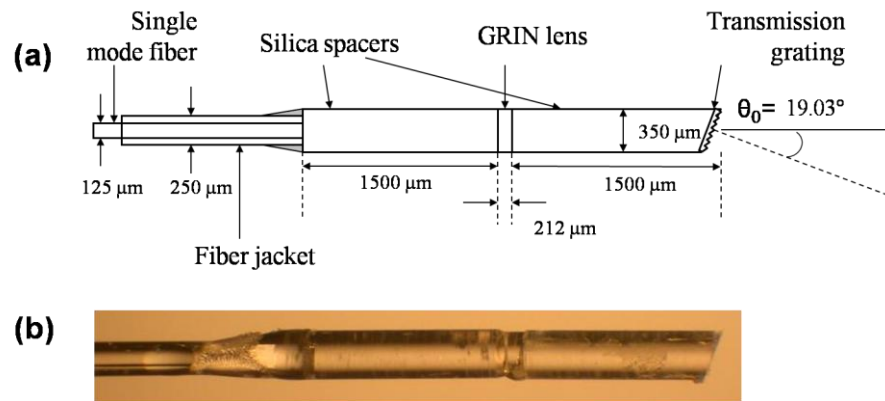

Fig. 2. (a) Schematic illustration of the SEE probe [6,14,15]. (b) A photograph of the probe.

3.2 Point-spread function

The main disadvantage of small diameter endoscopes is their inability to resolve large numbers of resolvable points that would be sufficient for demanding clinical applications. While it was previously noted [5] that SEE is capable of resolving more points than, for example, fiber bundle endoscopes of equivalent diameters, SEE resolution is also strongly dependant on the diameters of its optics, as spatial dispersion requires illumination of a large

number of grating lines. In order to derive the theoretical PSF of the SEE probe at the center of the field of view (FOV), we will assume that the beam emitted from the optical fiber over-fills the aperture of the GRIN lens, maximizing its effective numerical aperture, as well as the illuminated area of the grating. We assume that the lens is illuminated on its optical axis by a perfect spherical wave, and neglect optical aberrations, which will be addressed in detail in Sections 3.5-3.6.

Consider first a monochromatic point source P located at the fiber core, from which light propagates via a lens of diameter D and is deflected by a grating, as schematically depicted in Fig. 3. According to Fresnel diffraction theory, the field distribution E_M at the focal plane z_0 of the SEE probe for *monochromatic illumination* of angular wavenumber k_m, is given by:

$$E_M\left(k_m, x, y, z_0\right) = E_0\left(k_m\right) C k_m^2 e^{i\frac{k_m}{2z_0}\left(\left(x-x_m\right)^2 + y^2\right)} \left[\frac{J_1\left(k_m D \sqrt{\left(x-x_m\right)^2 + y^2}\Big/2z_0\right)}{k_m D \sqrt{\left(x-x_m\right)^2 + y^2}\Big/2z_0}\right], \quad (3)$$

where C denotes a scaling constant containing uniform spectral attenuations in the optical system, E_0 denotes the source field amplitude, and x_m denotes the location of the first diffraction order for k_m (Fig. 3, red solid lines). For simplicity, we will consider the field at $y=0$, and omit the y coordinate from the following equations.

For deriving the PSF, we consider a sample with a single point reflector of reflectivity r_0 located at x_s: $r_S\left(x\right) = r_0 \delta\left(x - x_s\right)$, where δ denotes the Dirac delta function. When the illumination field contains a continuum of wavelengths with a total bandwidth σ_k, the total amplitude of the illumination field at x_s is obtained by integrating over all angular wavenumbers: $E_S\left(x_s, z_0\right) = r_0 \int_{\sigma_k} dk_m E_M\left(k_m, x_s, z_0\right)$.
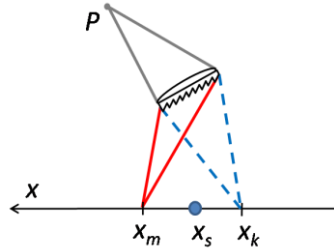

Fig. 3. Schematic illustration of the illumination and signal collection optical paths in SEE.

The back-reflected light propagation from the sample to the probe is governed by the same diffraction principles that are valid for the illumination, and the field collected by the fiber core from a point reflector at x_s for any wavenumber k is given by:

$$E_C\left(k, x_s, z_0\right) = C E_S\left(k, x_s, z_0\right) k^2 e^{i\frac{k}{2z_0}\left(x_s - x_k\right)^2} \left[\frac{J_1\left(kD\left|x_s - x_k\right|/2z_0\right)}{kD\left|x_s - x_k\right|/2z_0}\right], \quad (4)$$

where $E_C\left(k, x_s, z_0\right)$ denotes the collected monochromatic field and x_k denotes the location of the first diffraction order, corresponding to the angular wavenumber k (Fig. 3, blue dashed lines). The field $E_S\left(k, x_s, z_0\right)$ can be calculated using a "spectral overlap" function $f\left(k_m, k\right)$, which expresses the overlap between an illuminating channel k_m and a collection channel k:

$$E_S\left(k, x_s, z_0\right) = r_0 \int_{\sigma_k} dk_m E_M\left(k_m, x_s, z_0\right) f\left(k_m, k\right). \quad (5)$$

Using the single-mode fiber core as an effective pinhole, the SEE probe is essentially a *confocal* optical arrangement in which both the illumination and the collection optical paths overlap in space, i.e. $f(k_m, k) = \delta(k_m - k)$. Substituting $f(k_m, k)$, Eq. (2) and Eq. (5) into Eq. (4), we obtain, after a change of variables, the spectral distribution of the field returning from the sample to the fiber core:

$$E_C(k, k_s, z_0) = E_0(k) r_0 C^2 k^4 e^{i \frac{k}{z_0} \left(\frac{2\pi G z_0}{\cos\theta_0} \frac{k - k_s}{k^2} \right)^2} \left[\frac{J_1(\pi DG|k - k_s|/k \cos\theta_0)}{\pi DG|k - k_s|/k \cos\theta_0} \right]^2, \quad (6)$$

where k_s is the wavenumber whose first diffraction order is located at the scatterer location x_s, and where we have assumed that $\cos\theta \approx \cos\theta_0$ for the spectral region around the central wavelength at the center FOV.

The (field) PSF of SEE is thus given by:

$$h(k, k_s, z_0) = E_C(k, k_s, z_0) / (E_0(k) \cdot r_0), \quad (7)$$

and its full width at half maximum (FWHM) is given by: $\Delta k = 1.029 k \cos\theta_0 / DG$, and in terms of wavelength:

$$\Delta\lambda = 1.029 \frac{\lambda \cos\theta_0}{DG}. \quad (8)$$

The intensity PSF $|h(k)|^2$, has a FWHM given by $S_k = 0.738 k \cos\theta_0 / DG$, and in terms of spatial coordinates, using Eq. (2):

$$S_X = 0.738 \frac{\lambda z_0}{D}, \quad (9)$$

where the numerical coefficient was derived numerically from the intensity PSF. Due to the circular symmetry near the optical axis, a similar expression can be derived from Eq. (3) for the FWHM along the *y* axis: $S_Y = S_X$. Substituting the system's and probe's parameters from Ref [6]. into Eq. (9) yields $S_X(z_0 = 10\,\text{mm}) = 16.87\,\mu\text{m}$ at the central wavelength, representing the aberration-free, Fourier-limited system performance at the center FOV.

The spectral intensity PSF $|h(k)|^2$ and the spectral transfer function amplitude $|h(k)|$ are plotted in Fig. 4(a) around the central wavelength λ_0 = 800 nm (black solid line and black dashed line, respectively). These Airy patterns are the result of the circular aperture of the diffraction grating, and would have different geometries for different probe shapes and illuminating wavefronts. For example, some feasible SEE probe designs require the use of gratings with rectangular shapes, which could be easier to manufacture compared with circular or oval gratings. Such rectangular gratings produce different intensity PSF and transfer function curves, as illustrated by red markers in Fig. 4(a) for a square probe aperture, showing somewhat broader central spot and slightly more pronounced side lobes.

In a three-dimensional sample, the complex amplitude of the optical field $E_C(k)$ collected from the sample can be expressed as the coherent summation of all scatterers with reflectivities $r_S(x,z)$ within the illuminated *x-z* cross section, given by:

$$E_C(k) = E_0(k) \int_{\sigma_k} \int_{DOF} h(k, k_s) r_S(x(k_s), z) e^{2ik\bar{n}z} dz dk_s, \quad (10)$$

where DOF denotes the depth of focus (FWHM of the confocal axial PSF). We assume here that the transfer function *h*, previously calculated for the focal plane at z_0, remains

approximately unchanged within DOF. The distance z_0 is given by $z_0 = z_m + z_s$, where z_m and z_s denote the propagation distances in the medium and in the sample, respectively. For simplicity, we assumed that the probe optics have a total length that is much smaller than its working distance z_0, thus we can neglect phase accumulation inside the probe. This assumption is justified by realizing that the 1.5 mm separation between the lens and the grating (Fig. 2) is a result of the specific manufacturing process, and could be made much smaller in future versions of the probe. The weighted refractive index is given by $\tilde{n}(z_s) = (n_m z_m + n_s z_s)/z_0$, where n_m and n_s denote the refractive indices of the medium and the sample, respectively.
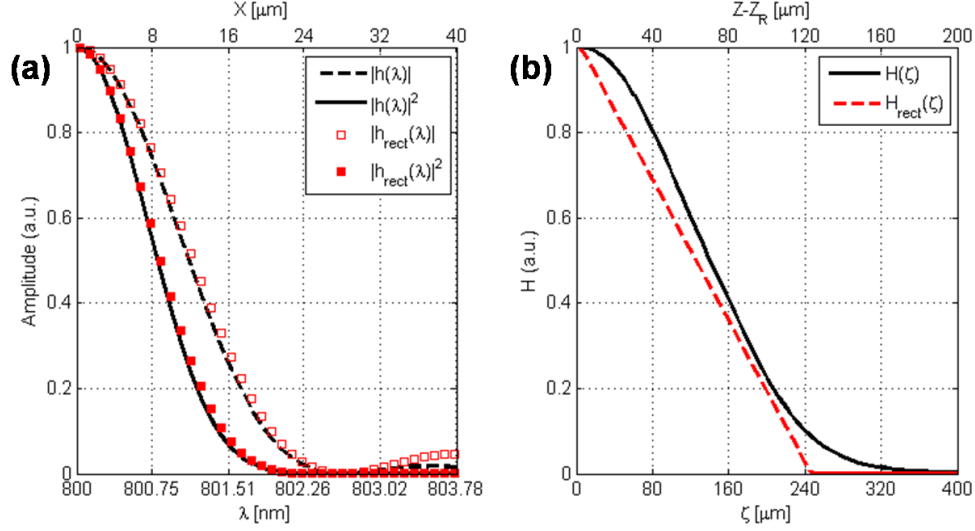

Fig. 4. (a) Lateral intensity PSF (black solid line) and the spectral impulse response $|h(\lambda)|$ (black dashed line) of SEE probe with a uniformly illuminated circular aperture and a working distance of 10 mm. A rectangular aperture produces a slightly different lateral spectral transfer function (hollow red squares) and PSF (filled red squares). (b) Interferometric axial PSF of confocal SEE (black solid) compared to the PSF of a confocal system with rectangular aperture (red dashed). The top axis axial coordinates assume $n_s = 1$.

In the reference arm, the complex amplitude of the optical field reflected from a mirror with reflectivity r_R is given by:

$$E_R(k) = E_0(k) r_R e^{2ikz_R}, \tag{11}$$

where z_R denotes the distance between the fiber exit and the reference mirror (Fig. 1). Constant attenuations in both arms were neglected for clarity. In order to calculate the interferometric axial PSF, we consider the spectral interference between the returning reference and sample signals, captured by the spectrometer line camera, which can be expressed as the coherent summation of the fields from the reference (Eq. (11)) and sample (Eq. (10)) arms:

$$I(k) = |E_R + E_S|^2 = |E_0(k)|^2 \left[r_R^2 + \left| \int_{\sigma_k} \int_{DOF} h(k,k_s) r_S(x(k_s),z) e^{2ik\tilde{n}z} dz dk_s \right|^2 \right.$$

$$\left. + 2r_R \operatorname{Re} \left\{ \int_{\sigma_k} \int_{DOF} h(k,k_s) r_S(x(k_s),z) e^{2ik(\tilde{n}z-z_R)} dz dk_s \right\} \right]. \tag{12}$$

The first term on the right hand side of Eq. (12) represents the intensity reflected from the reference arm, which could be experimentally measured by blocking the light returning from

the sample arm. The second term represents the self-interference of light from different axial scatterers within the sample, and the third term represents the cross-interference between the sample and reference fields, containing the cross-sectional distribution of the reflections within the sample.

At this point it is worth noting that by substituting $G = 0$ in Eq. (7) (meaning essentially no diffraction grating in the probe) we obtain from Eq. (12) an expression for the spectral interference in spectral domain OCT (SD-OCT) [16] (neglecting constant attenuation factors):

$$I_{OCT}(k) = |E_0(k)|^2 \cdot \left[r_R^2 + \left| \int_{DOF} r_S(z) e^{2ik\tilde{n}z} dz \right|^2 + 2r_R \int_{DOF} r_S(z) \cos(2k(\tilde{n}z - z_R)) dz \right], \quad (13)$$

where the sample reflectivity $r_S(z)$ is a function of the z coordinate only. OCT could be therefore viewed as private case of SEE, in the limit where the number of transverse resolvable points in SEE equals 1. A comparison between SD-OCT and SD-SEE has been previously described in Ref [14].

We may now neglect the phase term of the spectral transfer function $h(k, k_s)$ in Eq. (7) by noting that it changes very little (by approximately 0.2 radians) over its own spectral width Δk. The impulse response $h(k, k_s)$ [Eq. (7)] then becomes a real function, and the cross-interference term in Eq. (12) is given by:

$$I_{CI}(k) = 2r_R E_0^2 \int_{\sigma_k} \int_{DOF} h(k, k_s) r_S(x(k_s), z) \cos(k\zeta) dz dk_s, \quad (14)$$

where $\zeta = 2(\tilde{n}z - z_R)$ denotes the modulation frequency of the interference patterns on the spectrometer, and we have assumed that the source spectrum varies slowly over the entire width (Δk) of $h(k)$, hence $E_0(k) \approx E_0$. Equation (14) implies that the *axial* resolution is related to the spectral width of $h(k)$, which is related to the *lateral* PSF through the spatial coordinate encoding [Eq. (2)].

Using a single scatterer representation in the cross sectional *x-z* plane: $r_S(x, z) = r_S \delta(x) \delta(z - z_0)$ and substituting it into Eq. (14), we obtain:

$$I_{CI}(k) = 2r_R r_S(0, z_0) E_0^2 h(k - k_0) \cos(k\zeta_0), \quad (15)$$

where $\zeta_0 = 2(\tilde{n}z_0 - z_R)$. The optical path difference between light reflected from a single point at the sample, and from the reference mirror can now be calculated using a Fourier transformation of Eq. (15) over the entire spectral bandwidth σ_k:

$$I(\zeta) = I_0 \cdot FT\{I_{CI}(k)\} = I_0 \cdot H(\zeta) \otimes [\delta(\zeta - \zeta_0) + \delta(\zeta + \zeta_0)], \quad (16)$$

where $I_0 = 2E_0^2 \cdot r_R \cdot r_S(0, z_0)$, and $H(\zeta) \equiv FT\{h(k)\}$. The problem of depth ambiguity, manifested through the emergence of two axially symmetric images for each scatterer, is a result of the real-part only spectral measurement of the spectrometer, and could be solved by acquiring a second spectral measurement with the reference mirror relocated to induce a $\pi/2$ phase shift in the reference plane, and combining two spectral measurements to retrieve the complex spectral amplitude [9,14]. This technique would allow utilizing the full resolution power of the spectrometer and doubling the imaging depth range compared to a single spectral acquisition. In addition, similar techniques were shown useful in SD-OCT [17] for effectively removing the reference background and the effect of the sample self interference.

A plot of $I(\zeta)$ is shown in Fig. 4(b) for circular (black solid line) and rectangular (red dashed line) probe apertures. The triangular profile of the axial PSF in Fig. 4(b) is an interesting and unique feature of SEE, resulting from Fourier-transforming a sinc-squared function, which may suggest a possible resolution advantage over circular apertures in high SNR imaging conditions.

Solving Eq. (16) numerically, we obtain an expression for the FWHM of the axial PSF:

$$S_z = 0.45 \frac{DG\lambda_0}{n_s \cos\theta_0} = 0.463 \frac{\lambda_0^2}{n_s \Delta\lambda}. \tag{17}$$

We note that by replacing $\Delta\lambda$ with the total source bandwidth σ_λ, Eq. (17) can be used to approximate the axial resolution of OCT. Since SEE uses the spectrum primarily to encode space, its axial resolution is lower than that of OCT [14] by a factor approximately equal to the number of spectrally resolved spectral points $\sigma_\lambda/\Delta\lambda$. Substituting the system's and probe's parameters from Ref. [6]. into Eq. (17) yields $S_z \approx 135\,\mu m$, representing the aberration-free, Fourier-limited axial resolution at the central FOV.

3.3 Field of view

In order to obtain approximate analytical expressions for the field of view of SEE, we first simplify Eq. (1) by using the small angle approximation, $\sin\theta \approx \theta$, and by assuming that θ is linear with λ across the entire source spectrum σ_λ. Equation (2) would then hold for the entire lateral image area, i.e.:

$$\Delta X = \frac{Gz_0}{\cos\theta_0}\sigma_\lambda. \tag{18}$$

In the *y* axis, the field of view depends on the scanning angle of the galvanometric scanner (see Ref [9].). Applying a full, continuous 360° rotation of the probe using an optical rotary junction would allow maximizing the lateral field of view and could reduce mechanical vibrations. The geometry of the three dimensional field of view in this configuration is discussed in Section 3.6. In some clinical applications, continuous saw-tooth scanning of the rotation angle is desired in order to produce high frame rates at nearly rectangular fields of view. For small rotation angles, the lateral FOV in the *y* axis is given by:

$$\Delta Y = 2z_0 \tan(\Delta\varphi), \tag{19}$$

where $\Delta\varphi << \pi/2$ denotes the amplitude of the probe rotation angle (Fig. 1).

The axial imaging range of the SEE probe is limited by the spectrometer's ability to resolve high spectral modulation frequencies (denoted by ζ in Section 3.2). The total imaging range in the *z* axis is then derived from the Nyquist sampling limit and is given by:

$$\Delta Z = \frac{\lambda^2}{\Delta\lambda_{spec}}. \tag{20}$$

Note that the expression in Eq. (20) is independent on spectral encoding, and is valid for SD-OCT as well. The axial imaging range could be extended beyond this limit by stepping the reference mirror position between consecutive spectral acquisitions [9]. This approach would require sophisticated data acquisition and processing, and would eventually be limited by the total depth of focus of the probe's optics.

3.4 Resolvable points

The number of resolvable points is a critical parameter in small diameter endoscopes for evaluating the amount of information within a single image. In the spectrally encoded x axis, the number of resolvable points can be approximated by calculating the ratio between the field of view and the spatial resolution:

$$N_X = \frac{\Delta X}{S_X} = 1.355 \frac{\sigma_\lambda GD}{\lambda_0 \cos \theta_0}. \tag{21}$$

Similarly, for the y axis, the number of resolvable points is given by:

$$N_Y = \frac{\Delta Y}{S_Y} = 1.355 \frac{2D \tan(\Delta\varphi)}{\lambda_0}. \tag{22}$$

Similar expressions to those of Eqs. (21) and (22) have been used for estimating the number of resolvable points in previous works ([5,8,9]), the only difference being the numerical constant 1.355, which is a consequence of the smaller *confocal* lateral PSF. Overall, we find a total of $1.355^2 \cong 1.84$ increase in the number of resolvable points in the lateral plane compared to what was previously accepted for SEE.

The number of *axial* resolvable points in SEE is limited by the number of resolvable spectral modulation frequencies (ζ), which is equal to the number of resolvable elements $\Delta\lambda_{spec}$ within each bandwidth fraction $\Delta\lambda$ encoding each lateral resolvable element:

$$N_Z = \Delta\lambda/\Delta\lambda_{spec}. \tag{23}$$

For the parameters of the experimental system in Ref [6]. we obtain $N_X = 188$, $N_Y = 209$, and $N_Z = 22$. The theoretical number of resolvable points in the lateral x-y plane is ~ 1.5 times more than previously predicted [9,14].

Equation (21) and Eq. (23) are both derived from a single spectral acquisition. Using Eq. (8), the product of these expressions represents the single-shot total number of cross sectional (x-z plane) resolvable points:

$$N_X N_Z = 1.39 \frac{\sigma_\lambda}{\Delta\lambda_{spec}}. \tag{24}$$

Interestingly, the total number of resolvable points in the x-z plane is *independent of the optical parameters of the probe*, only on the source and spectrometer properties. Therefore, Eq. (24) represents a fundamental upper limit of the spectral encoding technique, implying that the spectral content of the SEE system eventually limits its imaging performance, operating as an 'information resource' for the system.

3.5 Optical aberrations

In the above analysis, Eqs. (9) and (17) express the transform-limited PSF width for the center wavelength at Littrow angle, and therefore represent the upper limit for the resolution for the SEE prototype system. Various optical aberrations are present in the current design of the SEE probe, which affect image quality, resolution, and field of view. In the following analysis, optical design software (ZEMAX Development Corporation, Washington, USA) was used to analyze several key imaging parameters, including the lateral PSF and focal plane geometry. A two-dimensional layout of the SEE probe and the light rays at three representative wavelengths are shown in Fig. 5. A close-up view of the rays within the probe (Fig. 5, inset) shows the diverging wave from the single-mode fiber over-fills the GRIN lens aperture, which slowly focuses the beam at the focal plane. The curved focal line, marked by a black solid line, connects axial points along the rays with the smallest diameter transverse spot. The

diffraction angle between the central wavelength (800 nm) and the probe's optical axis is 38°, which equals twice the Littrow's angle. The rest of the spectrum is diffracted around the central wavelength, generating a spectral line on the sample located approximately 10 mm from the grating. The properties of the simulated GRIN lens are summarized in Fig. 5.
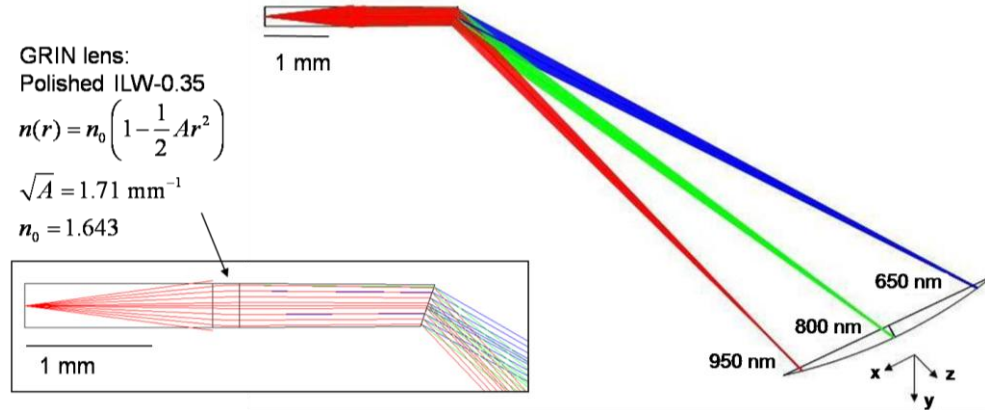

GRIN lens:
Polished ILW-0.35

$$n(r) = n_0 \left(1 - \frac{1}{2} A r^2 \right)$$

$$\sqrt{A} = 1.71 \text{ mm}^{-1}$$

$$n_0 = 1.643$$

Fig. 5. Simulations of the light rays illuminating the sample through the SEE probe. A magnified view of the probe's drawing is shown in the inset.

Due to the unique design of the probe optics, some optical aberrations are manifested in a different way than in conventional imaging systems. The effect of coma aberrations due to non-axial rays in the lens is practically nonexistent in the SEE probe since the broadband light emitted from the single mode fiber propagates only in the probe's optical axis and illuminates the lens axially. The spherical aberrations induced by the GRIN lens are also negligible due to the non-spherical surfaces of the lens. Based on ZEMAX simulations we estimate that spherical aberrations cause less than 0.5% broadening of the lateral PSF across the entire focal plane (data not shown).

In order to quantify and isolate the effect of chromatic aberrations, we have computed the focal shift and the spot size of the illumination rays for different wavelengths within the source spectral range without the presence of the grating, and with the distal surface of the probe perpendicular to the optical axis (not at Littrow's angle). The main effect of chromatic aberrations in SEE is evident on the axial location of the focal line (Fig. 6), where each wavelength is focused at different axial distance from the lens. We have calculated a focal plane tilt of approximately 8.5° in the x-z plane as a result of chromatic aberrations only.
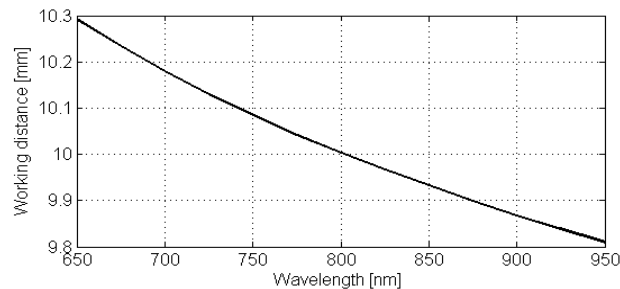

Fig. 6. Focal shift induced by chromatic aberrations for a working distance of 10 mm for the center wavelength.

We have found that chromatic aberrations impose approximately 1% (0.1 μm) broadening of the PSF. This negligible influence of chromatic aberrations on resolution results from the

relatively small bandwidth fraction $\Delta\lambda$ (Eq. (8)) illuminating each sample location, and may help in reducing the cost and complexity of future miniature lenses [18].

An additional asymmetric aberration in the focal plane is due to astigmatism caused primarily by the diffraction grating itself. When a slowly converging beam with radially symmetric cross-section is diffracted by a grating, its intensity cross-section becomes elliptical at any diffraction angle other than Littrow's. As a result, different curvatures along the x and y axes cause the beam to focus at different axial locations. To study the effect of astigmatism, we have simulated the transverse intensity profile of the beam for different axial locations and for several wavelengths, 25 nm apart within the source bandwidth. A plot of the focal shifts of the two foci in the x axis (green circles) and in the y axis (blue rectangles) as a function of wavelength is shown in Fig. 7(a), with the axial locations corresponding to maximum lateral circular symmetry (red triangles). The effect of chromatic aberrations is also evident in Fig. 7(a) through the focal tilt on y axis, where astigmatism is negligible. Also evident is the focal line curvature with radius of approximately z_0, which results from the grating angular dispersion, and could be perceived as the equivalent of the Petzval curvature of lenses and objectives.

In addition to inducing two different axial focal spots, astigmatism also affects lateral resolution by forming distinct spots having oval shapes with perpendicular main axes [Fig. 7(b), blue and green markers]. A theoretical spot size evaluation can be made using Eq. (9), where z_0 is replaced by $z_0(\lambda)$ taken from the best foci locations shown in Fig. 7(a). In addition, the working distances from the lens, including the length of the finite silica spacer, were taken into account. The resulting theoretical prediction [Fig. 7(b), red triangles] is within a good agreement with the simulation (ZEMAX) results.
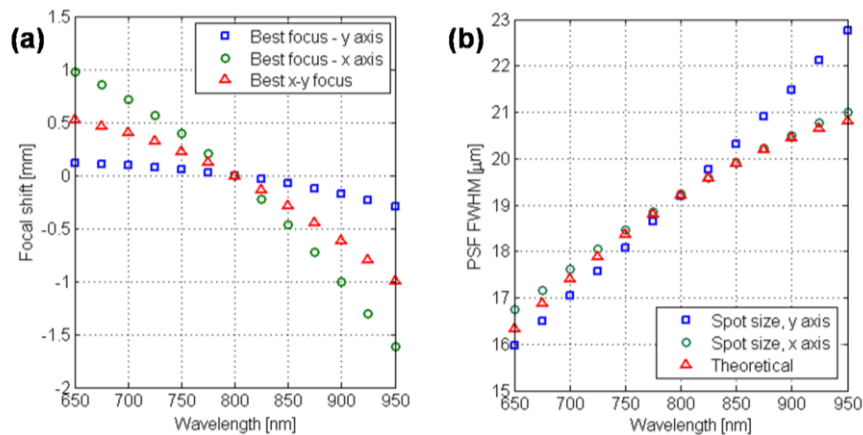

Fig. 7. (a) Focal shift of different wavelengths, showing the effect of astigmatism. (b) Intensity FWHM – actual focus in x and y dimensions, represented with the diffraction-limited resolution for comparison.

Another optical aberration that needs to be considered is caused by the minute field curvature of the beam illuminating the grating, which results in multiple effective illumination angles around θ_0. To analyze this effect, a probe configuration with 0.5 mm working distance was simulated [Fig. 8(a)]. Such probe design, which is capable of imaging at relatively high numerical apertures, is feasible simply by polishing down the grating substrate prior to probe assembly. The simulated probe produced significant broadening of the PSF in the x-axis [approximately 1.5 times wider than the y axis PSF, Fig. 8(b)]. Combined with the chromatic aberrations of the GRIN lens, which result in different beam curvatures for different wavelengths, this effect is also wavelength-dependant, and is more pronounced for long wavelengths which have shorter focal lengths. The PSF FWHM is plotted in the x and y axes

as a function of the working distance in Fig. 8(c), showing that this aberration becomes significant for short working distances, below 1.5 mm. Consequently, there is a limit to the maximum possible spatial resolution obtained with the distal-grating SEE configuration. High resolution spectrally encoded imaging is most suitable using confocal arrangement in which the imaging lens is the most distal element in the probe [19,20].
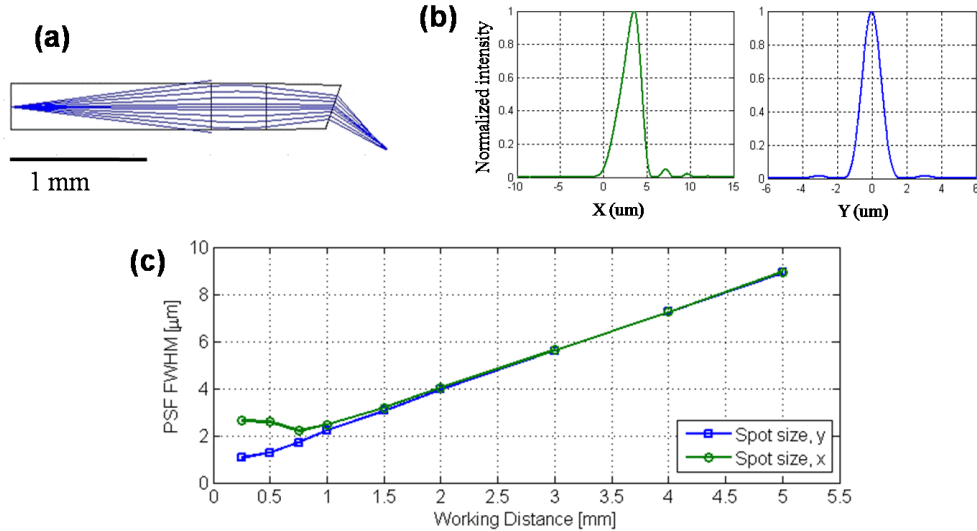

Fig. 8. (a) Schematic of an SEE probe with 0.5 mm working distance ($\lambda = 800$ nm). Note that the distal silica spacer is only 0.5 mm long. (b) The PSF in the x and y axes 0.5 mm from the grating. (c) The effect of working distance on the PSF in the x axis (green) and y axis (blue), resulting from the illuminating field curvature.

The cumulative effect of image curvature, chromatic aberration and astigmatism on the focal line in the x-z plane is summarized in Fig. 9, showing that the resulting focal plane (red dashed line) is tilted by approximately 25° (on average) from the aberration-free focal plane (solid green line) due to the combined effect of chromatic aberrations (8.5° tilt, dotted blue line) and astigmatism.
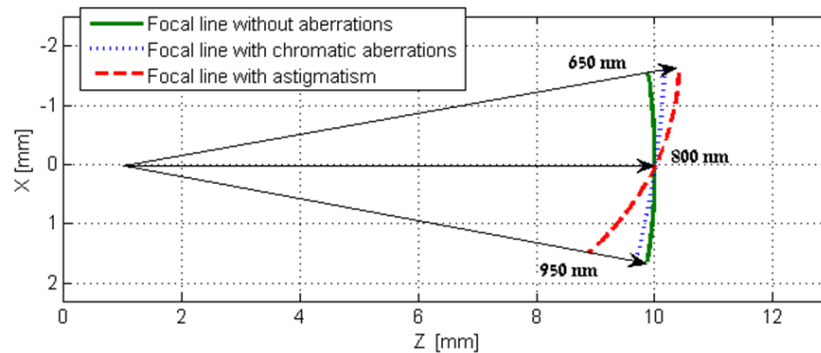

Fig. 9. The relative contribution of chromatic aberrations and astigmatism to the focal plane geometry.

3.6 Three-dimensional field of view

In order to model the three-dimensional FOV, we use Eqs. (18), (19) and (20) to obtain the FOV in the x, y, and z axes, respectively, and incorporate our optical aberrations analysis to

account for focal plane angle and curvature. The total effect of the unique optical configuration and optical aberration of SEE on the volumetric FOV is summarized in Fig. 10(a) for $\varphi = \pm 20°$ rotation angle. The focal plane [Fig. 10(b)] appears slightly curved due to the effects of both the Petzval image curvature (x axis) and probe rotation (y axis). In an x-z section [Fig. 10(c)], the strong tilt of the field due to chromatic aberrations and astigmatism is clearly visible, as well as the asymmetry in image depth due to the longer encoding wavelengths. Volumetric rendering of the FOV for a full probe rotation ($\varphi = 360°$) is shown in Fig. 10(d).
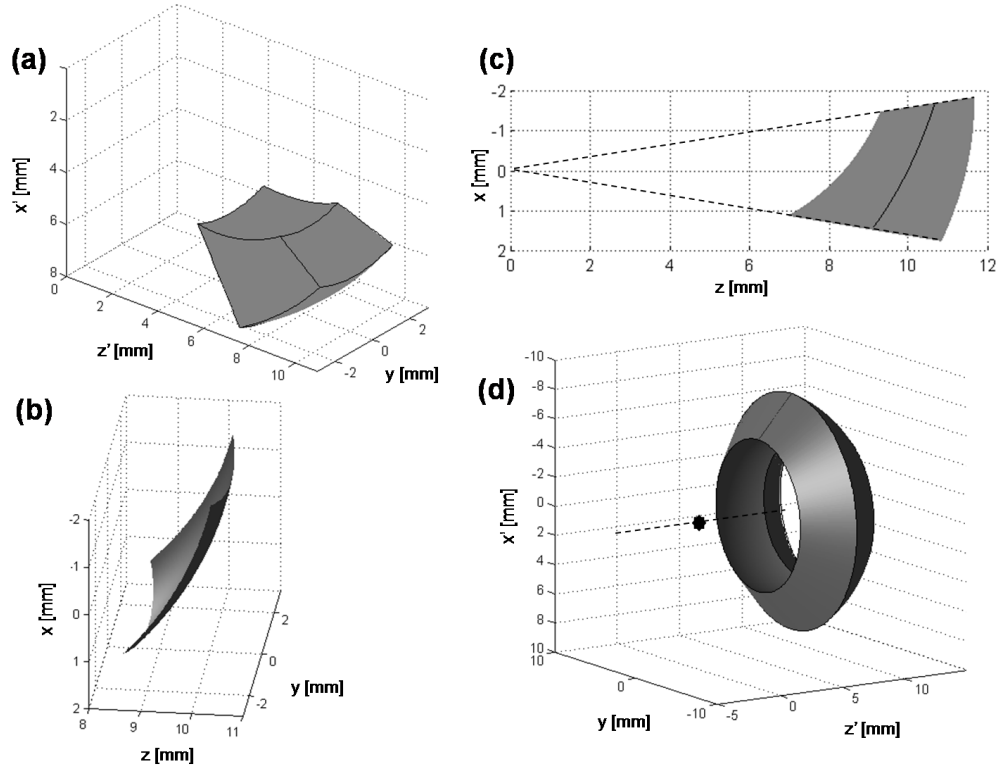

Fig. 10. The three-dimensional field of view of SEE: (a) Volumetric rendering of the FOV, with the probe at the origin, rotated by total angle of 40°. (b) Surface rendering of the focal plane for a 40° rotation angle. (c) An x-z cross section of the FOV at $y = 0$. (d) FOV with full probe rotation (probe location is marked by a star). The x' and z' axes in (a) and (d) define a new coordinate system rotated by $2\theta_0$ relative to the SEE focal plane.

4. Discussion

The use of high power diffraction grating for imaging within the confines of a small imaging probe, impose some unique imaging characteristics, as well as certain limitations on the optical performance of SEE. Since depth resolution in SEE is achieved using low coherence interferometry, confocal optical sectioning is generally an undesired effect, since it limits the total depth range of SEE [21]. The effect of the confocal arrangement on lateral resolution, however, leads to an increase of the number of resolvable points by a significant amount. Previous works [5,9] have underestimated the number of lateral resolvable points in the spectrally encoded axis: $N_X^{[5,9]} = (\sigma_\lambda GD)/(\lambda_0 \cos \theta_0)$, taking into consideration only the illumination optical path, and neglecting the confocal aperture. Our analysis [Eq. (21)]

predicts approximately 35% increase in the number of resolvable points in one lateral axis, almost doubling the number of points in the entire lateral image.

The theoretical increase in lateral number of resolvable points is partially counterbalanced by astigmatism, particularly at the FOV edges. Other aberrations have less pronounced impact: we have found that the lens coma, spherical and chromatic aberrations have negligible effect on resolution. The effect of grating illumination by a converging wavefront is negligible in SEE probes with relatively long focal lengths; however this aberration becomes more pronounced as the probe's numerical aperture is increased, essentially limiting the maximum resolution of the current probe configuration. Future sub-millimeter diameter probe designs with focal lengths shorter than 1.5 mm would require different optical configurations in order to maintain high resolution, for example, by using two lenses in the probe, first for collimating the beam illuminating the grating, and second for imaging.

In the axial (z) dimension, the resolution is half the coherence length of the illuminating local bandwidth, approximately 135 μm in the current system-probe design. Such resolution is useful for identifying surface features such as tumor nodules [6], identifying anatomical landmarks, imaging subsurface tissue structures up to two millimeter below the surface [14], and for orientation in space. An interesting result of our theoretical analysis is that the rather unique relation between the spectral PSF and the axial PSF leads to a triangle-shaped axial response for rectangular probe apertures. It is worth noting that the approximation of the axial PSF by a triangular shape depends on fully capturing $h(k)$, including its far-extending side-lobes, which spans over the entire source bandwidth. Triangular PSF would potentially improve the effective axial resolution of interferometric SEE in specific high SNR imaging applications. The coupling between the lateral and axial dimensions also results with a fundamental limit on the number of resolvable points in the cross sectional (x-z) plane: since the total bandwidth σ_λ is used to encode space, the system's ability to *decode* the image ($\Delta\lambda_{spec}$) would dictate the amount of recovered information. The confocal arrangement, though, allows using the bandwidth more efficiently, as is evident from the 39% increase in resolvable points [Eq. (24)]. This factor results from the different way of encoding in each dimension: while the lateral resolution is proportional to the confocal intensity distribution $|h(k)|^2$, the axial resolution is a result of coherent summation, hence is proportional to the complex (and broader) $h(k)$ [Eq. (7)].

The optical design of the SEE probe also affects the focal plane geometry, and, as a result, its entire imaging volume. While the deviations of the focal plane from flat surface [see, for example, Fig. 10(b)] could be compensated numerically by straightforward volumetric data processing, the tilt of the entire FOV [at Littrow's angle, see Fig. 10(c)–10(d)] would be limiting for various clinical applications. Forward-looking spectrally encoded confocal microscopy probes has been demonstrated, using a lens-grating-lens arrangement [19,20], a configuration which was not considered in this work. Such configuration would be difficult to implement in sub-millimeter diameter endoscopes.

In summary, we have thoroughly analyzed several key imaging parameters of SEE, derived explicit expressions which formulate its resolution and field of view geometries in three dimensions, and outlined the system's unique optical aberrations. This analysis could be useful in understanding future system and probe designs, and would hopefully assist in the development of novel spectrally encoded imaging concepts.